

Reflection of linear internal tides from realistic topography: The Tasman continental slope

JODY M. KLYMAK, *

The University of Victoria, Victoria, Canada

Harper L. Simmons and Dmitry Braznikov

Affiliation, City, State/Province, Country

Samuel Kelly

Affiliation, City, State/Province, Country

Jennifer A. MacKinnon, Matthew H. Alford, and Robert Pinkel

Affiliation, City, State/Province, Country

Jonathan D. Nash

Affiliation, City, State/Province, Country

* Corresponding author address: Jody Klymak, University of Victoria, Victoria, BC, Canada

E-mail: jklymak@uvic.ca

ABSTRACT

9 The reflection of a low-mode incident internal tide on the Tasman continental slope is investigated using
10 simulations of realistic and simplified topographies. The majority of the slope is super-critical to the in-
11 ternal tide, which should predict a large fraction of energy reflected. However, the response to the slope
12 is complicated by a number of factors. The incoming beam is confined in space; it impacts the slope at
13 an angle; there is a roughly cylindrical rise directly offshore of the slope; and a leaky slope-mode wave is
14 excited. These effects are isolated in simulations that significantly simplify the topography. Determining a
15 reflected signal from an incident one is non-trivial, even in a numerical model, and the technique used here
16 is to remove the reflecting bathymetry from the simulation and subtract an incident response from the total
17 response to arrive at a reflected signal. Overall, the real slope reflects approximately 65% of the mode-1
18 internal tide as a mode-1 signal, which is less than two-dimensional linear calculations would predict, likely
19 due to three-dimensional concavity of the topography. It is also less than recent glider estimates, likely due
20 to along-slope inhomogeneity. A synthetic three-point mooring array can predict almost any reflectivity
21 because of spatial inhomogeneity. The inhomogeneity of the response comes from the Tasman Rise which
22 diffracts the incoming tidal beam into two beams, one focused downstream, and one diffracted to the north,
23 with a substantial null in incoming energy between them. Along-slope inhomogeneity is enhanced by a par-
24 tially trapped super-inertial slope wave that propagates along the continental slope, removing energy from
25 the internal tide in some spots and re-radiating it further north. This wave is present even in a simplified
26 straight-shelf topography, and its character can be predicted from linear resonance theory.

27 1. Introduction

28 Energy is lost from the surface tide when it interacts with topography, and in the deep ocean is largely
29 redistributed as an internal tide. The fate of the internal tide is unclear, but depends on the dominant
30 wavelengths that are forced. Gentle topography that is subcritical to the internal tide is likely dominated by
31 higher vertical modes and is thought to break via wave-wave interactions relatively close to the topography
32 (i.e. Polzin 2009; St. Laurent and Garrett 2002). Steeper supercritical topography, while exhibiting signif-
33 icant local dissipation, tends to radiate a large fraction of the internal tide away from the topography as
34 low-mode waves (i.e. at Hawaii Klymak et al. 2006; Carter et al. 2008). Given that a significant fraction of
35 the internal tide energy is generated at steep topography (Legg and Klymak 2008), and that the distribution
36 of the mixing it eventually drives has impacts on understanding the distribution of ocean properties and the
37 strength of the overturning circulation (i.e. Melet et al. 2013), it is desirable to understand where and how
38 the radiated energy dissipates.

One candidate sink for the low-mode internal tide is reflection, scattering, and dissipation from continental slopes. These slopes are known to be hotspots of turbulent mixing from the few observational studies to date (Nash et al. 2007; Klymak et al. 2011; Martini et al. 2013). However, these studies have also demonstrated some of the difficulties in tracking internal tide energy on these slopes. Net internal-tide fluxes are relatively straight forward to measure, but ideally we would like to separate the incident and reflected fluxes if a parameterization of turbulence on the slope is to be made since the incident fluxes are what drive the turbulence. The reflectivity of a continental slope is basically the ratio of the energy flux convergence divided by the total incident flux:

$$R = \frac{F_{out}}{F_{in}},$$

39 where F is depth integrated for a two-dimensional budget or line-integrated for a three-dimensional one.
40 Even simple two-dimensional linear models of reflection indicate that determining the reflectivity will be
41 challenging, with reflection co-efficients strongly depending on the modal content and phases of the incident
42 internal tides (Klymak et al. 2011) and the local surface tide (Kelly and Nash 2010). These linear models
43 have been used globally to estimate reflection co-efficients for the mode-1 tides on realistic continental slope
44 bathymetries, (Kelly et al. 2013a,b), but these calculations assume the incoming tide is known, and that the

45 slope is relatively homogenous over a distance similar to the mode-1 horizontal wavelength.

46 Determining the incident flux, F_{in} , from field data, and even from a numerical model with sufficient
47 complexity, is not trivial. In two dimensions, or with simple plane wave geometries, it is relatively easy to
48 fit incident and reflected plane waves and recover the desired reflection co-efficient (figure 1a). In the real
49 ocean, even if the tidal components can be easily separated from confounding influences, internal tides are
50 often spatially inhomogeneous, and form lateral “beams” (in x-y) that make plane wave fits difficult from
51 a finite array of moorings; for instance a mooring array could be located more in the incoming beam than
52 the reflected, leading to an exaggeration of the computed energy convergence (figure 1b). Plane-wave fits
53 to satellite altimetry tracks are promising, but will also suffer from a lack of fidelity if the internal tides are
54 inhomogeneous on the scale of the plane wave fits (Zhao and Alford 2009). In the model, high resolution
55 temporal and spatial information makes it possible to separate signals spectrally according to their direction
56 of propagation (i.e. using a Hilbert transform, Mercier et al. 2008), but this method works best if there are
57 no boundaries and the signals at the edges of the model domain can be tapered to reduce Gibbs ringing,
58 neither of which are applicable here.

59 The region considered here is the Tasman continental slope, and is the focus of a concentrated internal
60 tide field experiment. As preliminary work, it has been sampled continuously by gliders for many months in
61 2012 and 2013 (Johnston et al. 2015). The gliders were flown to form internal waves antennae over which
62 internal plane-wave fits were made. These efforts show a clear standing wave pattern, with amplitudes and
63 phases as one would expect for internal waves incident on the slope from the southeast where internal tides
64 are expected to be generated from the Macquarie Ridge (figure 2a). The amplitudes of the interfering waves
65 were such that the reflectivity is predicted to be high on this slope, with estimates of 0.7 to 1.0 from the
66 arrays (Johnston et al. 2015). The gliders also picked up a 100-km wavelength wave propagating along slope
67 towards the north, a finding we isolate and discuss below.

68 Here we run numerical simulations that are meant to represent a mode-1 internal M_2 tide incident on the
69 Tasman Slope, east of Tasmania. The simulations are only forced by the incident internal tide, and there is
70 no local forcing, allowing the reflection to be isolated. After discussing the model setup section 2, we briefly
71 consider the response this forcing has on the slope section 3 and compute and energy budget of the complete

72 response. In order to separate the physics of the reflection, we then simplify the geometry section 4, both
73 geometrically, and by removing parts of the topography. This technique allows us to separate incident and
74 reflected signals from the total response without appeal to simplified wavefits. We end with a discussion of
75 the results (section 5) where we note the applicability of two-dimensional reflection models and discuss the
76 leaky slope waves evident in the simulations. We conclude with a summary (section 6).

77 2. Model setup

78 a. Basics

79 The numerical model used here is the MITGCM (Marshall et al. 2006). The setup is very similar
80 to Buijsman et al. (2014), with the model run in hydrostatic mode, background (isotropic) diffusivities
81 and viscosities of $10^{-5} \text{ m}^2 \text{s}^{-1}$, and enhanced diffusivity and viscosity in regions of temporarily unstable
82 stratification, as in Klymak and Legg (2010). A second-order flux-limiting temperature advection scheme is
83 used which results in some numerical dissipation and diffusion. Tests were run with weaker forcing, and the
84 fraction of energy dissipated did not change in the simulations, indicating that the dissipation highlighted
85 below is heavily influenced by numerical dissipation due to the lack of lateral resolution (1 km). Dissipation
86 is not the main focus of this paper, and finer resolutions have been used for more focused efforts dealing
87 with turbulence on the slope (in preparation). These simulations are therefore the most “linear” that the
88 resolution will allow.

89 Topography is from a data set that combines Smith and Sandwell (1997) and multibeam data from
90 Australian surveys (Whiteway 2009) (figure 2b). For this paper, we use a Cartesian co-ordinate system
91 centered at 44S, 148 E, with y pointing 12 degrees east of geographic north (magenta lines, figure 2). This
92 co-ordinate system is close to cross-slope in the x-direction, and is used for conceptual convenience. The
93 simulations are run on a f-plane ($f = -10^{-4} \text{ s}^{-1}$), so no planetary beta effect has been included.

94 Relatively high lateral resolution is used along the continental slope (figure 3a, smallest inset green box)
95 of $\delta x = \delta y = 1 \text{ km}$. Resolution is expanded by 3.5% per grid cell beyond the high-resolution region, to a
96 maximum of 5 km in the second largest inset box (figure 3a); this keeps the resolution over the Tasman Rise

97 and the rest of the continental slope at least 5 km. Further out, the grid spacing is again increased at 3.5%
 98 per grid cell until a maximum grid cell size of 10 km is reached.

99 Vertical resolution is approximately stretched so $dz \sim N$, where $N^2(z) = -\frac{g}{\rho_0} \frac{d\rho}{dz}$ is the vertical stratifi-
 100 cation. 200 vertical grid cells are used for these simulations. The vertical stratification is from the World
 101 Ocean Atlas for the Tasman Sea just offshore of Tasmania (Boyer et al. 2013), and is assumed laterally
 102 constant in the domain. This precludes any mesoscale effects, which are believed to be important in this
 103 area, and are the subject of future work.

104 *b. Forcing*

105 To simplify the generation problem we apply an analytical forcing to our model. This is composed of
 106 two line sources at approximately the location of the Macquarie Ridge (figure 3a). The initial conditions
 107 and the southern and eastern boundaries of the model were set with this forcing. The forcing is similar to
 108 that suggested by Rainville et al. (2010), except instead of a single point source placed a distance R from
 109 the line source, the line source is digitized as a number of discrete point sources and their response in the
 110 domain summed. The mode-1 pressure anomaly is given by:

$$111 p'(x, y, t) = \sum_{i=1}^N a_i \exp(j(|k_t|r_i - \omega t)) \quad (1)$$

112 where $r_i = \sqrt{(x - x_i)^2 + (y - y_i)^2}$ is the distance to the source, and $|k_t|$ is the absolute value of the mode-1
 wavenumber:

$$113 k_t = \frac{(\omega^2 - f^2)^{1/2}}{c_e} \quad (2)$$

114 where ω is the frequency of the tide, f is the Coriolis frequency, and c_e is the eigenspeed of the vertical mode
 equation:

$$115 \frac{d}{dz} \left(\frac{1}{N^2} \frac{d\psi}{dz} \right) + \frac{1}{c_e^2} \psi(z) = 0. \quad (3)$$

116 Here $\psi(z)$ is the eigenfunction that sets the shape of the vertical mode, and the boundary conditions are
 $d\psi/dz = 0$ at $z = 0$ and $z = -H$, where H is the water depth. For convenience, we normalize $\psi_m(z)$ so that

$$117 \int_{-H}^0 \psi_m(z) \psi_n(z) dz = \delta(m - n). \quad (4)$$

117 Horizontal velocities can be linearly decomposed by these shapes, as can the pressure signal.

118 To compute the wavefield, the horizontal velocity components are derived from the internal wave consis-
119 tency relations:

$$u(x, y, t) = \sum_{i=1}^N \frac{k_x \omega + j k_y f}{\omega^2 - f^2} \frac{p'_i}{\rho} \quad (5)$$

$$v(x, y, t) = \sum_{i=1}^N \frac{k_y \omega - j k_x f}{\omega^2 - f^2} \frac{p'_i}{\rho} \quad (6)$$

120 where $k_x = k_t \cos(\theta_i)$ and $k_y = k_t \sin(\theta_i)$ are calculated from the angle to each element of the line sources
121 $\theta_i = \arctan((y - y_i)/(x - x_i))$.

122 The resulting incoming wavefield (figure 3a) has a beam of energy flux that radiates northwest, and is
123 relatively tightly focused. The interference pattern creates a null to the south and north, and a secondary
124 beam that radiates due west. This schematic agrees with more realistic regional tidal models (H. Simmons,
125 in preparation), and the amplitude of the beam was tuned to give approximately 7 kW m^{-1} of flux incident
126 at Tasmania in the pictured realization. The runs below were scaled to have weaker (more linear) fluxes,
127 with approximately 2 kW m^{-1} at Tasmania, but exactly the same spatial pattern. The initial condition is
128 applied uniformly through the domain, regardless of bathymetry, so there are some start-up transients as
129 the proper baroclinic flow develops.

130 This forcing is applied on the eastern and southern boundaries of the domain. The northern and western
131 boundaries are sponges where the velocity is slowly dropped to zero and the stratification relaxed to the
132 initial stratification (figure 3a, green rectangles). Our main focus is the area from $y=0$ to 400 km, so the
133 boundaries are sufficiently far that small residual reflections do not affect the response.

134 The ideal response off the Tasman topography would be as a plane-wave reflection from a wall at $x = 0$ km
135 (i.e. Johnston et al. 2015). Here we have a relatively confined beam, but we can make a start by considering
136 the reflection the beam from a wall at $x = 0$ km for $y > 0$ km (figure 3b,c) using the method of images
137 with identical line sources mirrored about the y-axis, and their phase shifted by 180 deg. The reflection
138 pattern that sets up is not entirely regular, but has some straight-forward features. The incoming beam
139 impacts the wall at approximately 30 deg. The horizontal wavelength of an M_2 internal tide is 178 km, so
140 the standing wave in the x-direction will have a wavelength $178/\cos(30) \approx 200$ km and in the y-direction

141 will have a wavelength of approximately 350 km. These spatial scales are readily apparent in the analytical
142 forcing despite the non-plane-wave character of the idealized forcing (figure 3c). Note that the standing
143 energy flux (figure 3b) has peaks and nulls in absolute value, with the peaks having large flux to the north.
144 The peaks are every half cross-slope wavelength (i.e. 100 km). The nulls have weak southward energy flux
145 (though it is difficult to discern from the subsampled arrows in the plot).

146 3. Realistic model simulation

147 The response of the forcing in the most complex domain motivates the more idealized experiments that
148 follow. From the initial forcing (figure 4a), a complex wavefield develops with clear scattering from the
149 Tasman Rise, the shelf, and numerous small inhomogeneities on the sea floor (figure 4b–d). Looking along
150 shelf, the phase of the velocity signal can be seen changing approximately every 200 km, and it changes
151 approximately every 100 km offshelf.

152 This sets up a complicated interference pattern that shows inconsistent cross-slope fluxes and peaks and
153 nulls in the along-slope fluxes to the north, as we might expect from an oblique standing wave (compare
154 figure 4h to figure 3b). However the pattern is complicated, with offshore peaks at approximately the correct
155 spacing offshore, but not lining up precisely in the north-south direction. There are inhomogeneities in the
156 energy that are not accounted for by a simple two-wave model.

157 A time-averaged energy balance is performed on the model using the terms outlined in Kang and Fringer
158 (2012); Kang (2011). Their energy balance vertically integrated can be schematized as:

$$159 dE_{bc}/dt = -\nabla_H \mathbf{F}_{bc} + \text{Conversion} - \text{Dissipation}. \quad (7)$$

160 where E_{bc} is the depth-integrated baroclinic energy density, \mathbf{F}_{bc} is the depth integrated energy flux, including
161 both the pressure work term and the non-linear advection of energy (which is small in our runs). All quantities
162 are averaged over an M_2 tidal period. “Conversion” is a complex term representing transfer from barotropic
163 motions to baroclinic (Kang 2011, eq. 5.102) and includes the barotropic heaving of the water column, the
164 density anomaly, and a non-linear horizontal advection term. The non-linear terms can be non-trivial in real
bathymetry (Buijsman et al. 2014). The conversion term is positive if the barotropic tide loses energy and

165 the baroclinic tide gains energy. “Dissipation” is computed here as the residual, and includes dissipation
166 due to interior viscosity, numerical dissipation, bottom drag, and diffusion of energy (small).

167 Of note in the energy calculation is that the largest local term in the energy budget is an alternating
168 pattern of barotropic-baroclinic conversion at the shelf break balanced by baroclinic flux convergences and
169 divergences (figure 5). The importance of the barotropic-baroclinic term can also be seen by considering the
170 x-integral of the energy budget from $x = -50$ km to $+100$ km (figure 6). Recall that the simulations have
171 no barotropic forcing. This coupling is catalyzed by a start-up transient hitting the slope with the incoming
172 internal tide beam, and continues throughout the simulation, and is a leaky super-inertial slope wave (see
173 section 5).

174 The time series of the energy terms integrated along the shelf demonstrates that the barotropic-to-
175 baroclinic term is relatively small when averaged, with a small loss of energy from the baroclinic tide to the
176 barotropic in the integral region (figure 6b). The model is largely in a steady state by tidal cycle 15, with
177 some residual oscillations in dE/dt and the flux convergence. The large-scale baroclinic energy changes do
178 not change the dissipation residual very much, which is relatively constant after 5 tidal cycles. To put the
179 50 MW of dissipation into context, the initial energy that comes in the east and south sides of this analysis
180 box in the initial conditions is 315 MW, so the model is dissipation about 17% of the incoming energy.
181 However, note that the dissipation is not the focus of these model runs nor of this paper. The forcing here
182 is approximately a factor 3 lower than the real forcing, so its likely the fraction of dissipation at this site is
183 higher (probably closer to 25%) if real forcing is used.

184 The majority of the energy budget is in the first vertical mode (figure 6c). Net fluxes in the region directly
185 offshore of the shelf break ($0 < x < 80$ km, and $0 < y < 400$ km) are composed of substantial mode-1 energy
186 converging on the shelf (95 MW net), and some reflected energy escaping in higher modes (28.3 MW, mostly
187 in modes 2–4). The 95 MW net flux is made up of the incoming and reflected mode-1 energy, and separating
188 those fractions out is the subject of the next section. There is some incoming higher-mode energy as well
189 due to scattering from the Tasman Rise, but as we will also show below, this is minor. The spatial pattern
190 (not shown) of the mode conversion at the continental slope indicates hot-spots for conversion. Modes 2 and
191 4 have a hotspot of conversion near $y = 250$ km, and Mode 3 at $y = 325$ km.

192 4. Simplified geometries

193 To help tease apart the effects of the Tasman Rise and the non-uniform shelf, we carry out a few simplified
194 geometric experiments (figure 7;figure 8). The REAL case is the one discussed above (figure 8f). The NO
195 TOPO case has no topography at all (figure 8a), just the beam being forced at the south and east boundaries
196 and (mostly) absorbed at the west and north. RISE was run with the real bathymetry west of $x = 70$ km
197 (figure 8e). Three idealized geometries simplify the physics even more: the SHELF case has a supercritical
198 two-dimensional continental shelf running north from $y = 0$ km(figure 8d). ROUND RISE is a 1700-m tall
199 cylinder-shaped bump with radius of 50 km centered at approximately the same location as the Tasman Rise,
200 with no shelf to the west (figure 8b). The simplified shelf and the rise are both used in the SHELF/RISE case
201 (figure 8c).

202 a. Shelf-only configuration

203 The simplest topography is the SHELF configuration (figure 8d). Here we have a response that is quite
204 similar to the analytical response calculated above (figure 3b). The only difference between these two cases
205 is the narrow shelf west of $x = 0$ km and the slight slope to the continental slope. The interference pattern
206 between the incoming wave and the reflected wave is clear in this plot, with the same characteristic length
207 scales as above, and a slight bending of the response due to the radial spreading of the beam.

208 The goal of this paper is to determine the amount of reflectivity of the continental slope. This is a hard
209 number to determine in a complicated geometry, and naturally depends on the region of integration. For
210 the SHELF configuration the situation is relatively simple, and we use it to illustrate the numerical technique
211 used below. The signal in the full simulation is assumed to consist of an “incoming” signal and a reflected
212 signal, so we can decompose the east-west velocity amplitude of the first vertical mode (for example) as:

$$u_1^t(x, y) = u_1^i + u_1^r \quad (8)$$

$$v_1^t(x, y) = v_1^i + v_1^r \quad (9)$$

$$p_1^t(x, y) = p_1^i + p_1^r \quad (10)$$

213 where u_1^t is the complex amplitude of the M_2 , mode-1 east-west velocity of the simulation with the reflection,

²¹⁴ u_1^i of the incoming signal, and u_1^r of the reflected signal. We assume for this example that the incoming
²¹⁵ signal u_1^i is given by the No TOPO simulation, and u_1^t is from the SHELF simulation. The reflected signal u_1^r
²¹⁶ is simply the difference of these two. This method has been used by Hall et al. (2013) for a two dimensional
²¹⁷ flow. Here it is an absolute necessity because of the complicated three-dimensional topography.

²¹⁸ In order to compute and energy budget, we consider that the energy fluxes are calculated from the
²¹⁹ decomposed signals as:

$$P_{u1}^t = u_1^t p_1^t \quad (11)$$

$$= \overbrace{u_1^i p_1^i}^{Incoming} + \overbrace{u_1^r p_1^r}^{Reflected} + \overbrace{u_1^i p_1^r + u_1^r p_1^i}^{Cross Terms} \quad (12)$$

$$P_{v1}^t = v_1^t p_1^t \quad (13)$$

$$= \overbrace{v_1^i p_1^i}^{Incoming} + \overbrace{v_1^r p_1^r}^{Reflected} + \overbrace{v_1^i p_1^r + v_1^r p_1^i}^{Cross Terms} \quad (14)$$

²²⁰ The cross terms are not negligible for any realistic forcing, and indeed give rise to the interference patterns
²²¹ seen above (Nash et al. 2004; Martini et al. 2007).

²²² The “total” response (figure 9d) consists of the incoming response (figure 9a), and the “reflected” signal
²²³ (figure 9b), and substantial cross-terms (figure 9c). The cross terms are mostly perpendicular to the direction
²²⁴ of reflection (i.e. parallel to the shelf) and alternate fluxing energy to the north and south every half cross-
²²⁵ shelf wavelength. Combined, these three components give the “total” flux with net fluxes to the north in
²²⁶ alternating peaks every full offslope wavelength.

²²⁷ The reflected response (figure 9b) shows approximately what we would expect with energy being radiated
²²⁸ to the north-east. There is some concentration of this energy at $y \approx 75\text{km}$, and $y \approx 225\text{km}$. As above, this
²²⁹ is because of coupling with a partially trapped slope wave that is forced by the internal tide. This coupling
²³⁰ causes a redistribution of the reflected energy, focusing it approximately every along-slope wavelength of the
²³¹ shelf wave (we show below that this wavelength changes as the shelf geometry changes).

²³² Performing this analysis for the lowest 10 modes, we arrive at an energy budget for the shelf in the green
²³³ box in the figures ($0 < y < 400\text{ km}$, and $x < 80\text{ km}$; figure 9, inset budgets). Note that we assume the
²³⁴ flux through $x = 0$ is zero. With this calculation, we see that 408 MW is incident on the shelf in mode-1.
²³⁵ There is also a net flux of 50 MW into this region from the cross terms. This is a redistribution of energy

236 from north of our box into the box. There is a net convergence of this cross-term energy because there is
237 dissipation in the box; in a purely inviscid solution this term should balance to zero over a closed box. If we
238 extend the integration further north, the cross-term flux drops to zero.

239 Most of the incoming energy reflects back out of the box (figure 9b), with the bulk remaining in mode
240 1, and some scattering to higher modes. This scattered energy reflects to the north east (not shown). The
241 mode-1 reflection is affected by a shelf wave that transfers energy to and from the barotropic tide along the
242 slope, resulting in nulls and peaks in the mode-1 reflection.

243 *b. Tasman Rise only*

244 The Tasman Rise has a profound effect on the energy that impacts the continental slope, as well as
245 having some back reflection (figure 8e and f). The incoming beam is almost 500 km wide at $x = 0$ if there is
246 no Tasman Rise, but breaks into three narrower beams when there is a Tasman Rise (figure 8e). Upstream
247 of the rise, the effect is somewhat less energy propagating westward, with an interference pattern towards
248 the east indicating some back reflection.

249 This pattern can be explained in terms of diffraction of the internal tide beam from a deep obstacle (i.e.
250 Johnston and Merrifield 2003). There is a down-wave concentration of energy along the seamount's axis,
251 a null, and sidelobes to the north and south. In this case, the incident beam is of comparable size to the
252 obstacle, leading to an asymmetry, and a stronger lobe to the north than south.

253 Most of the response due to the Tasman Rise can be modeled simply as a cylindrical obstacle in the
254 beam (figure 8b and c). Here our obstacle is 1800 m high in 5000 m of water, and has a radius of 50 km
255 (figure 7). This captures most of the features of the actual Tasman Rise, despite not having a shallow spire
256 in the center and being slightly smaller than the real Rise. The differences make the simplified response
257 have weaker nulls and the whole response is directed a bit further north than the real Rise. Adding the shelf
258 (figure 8c) yields a response that bears substantial similarity to the REAL forcing case.

259 Decomposing into an incoming and reflected signal (figure 10) demonstrates the effect of the Tasman
260 Rise on the response. Less energy is incident on the control volume, largely because the diffraction redirects
261 some of that energy to the north of $y = 400$ km. There is a strong reflection of energy where the main

262 diffraction lobe reflects from the slope (figure 10b), and a smaller maximum just to the north ($y = 250$ km)
263 due to the along-shelf wave that is strummed. There is a reflection further north where the northern lobe of
264 the diffraction pattern reflects.

265 The incoming energy has some more high-mode content due to scattering at the cylindrical rise (fig-
266 ure 10a), though it is still 95% mode-1. The reflection is almost 80% mode-1, with some scattering to higher
267 modes. The net flux shows approximately 15% of the incoming energy is dissipated at the shelf.

268 *c. Real Case*

269 The REAL forcing is similar, if more complex (figure 11). The simulation using the bathymetry in the
270 RISE ONLY case (figure 8e) is used as the “Incoming” energy flux, and the REAL (figure 8f) case is the
271 “Total”. Compared to the cylindrical rise, the real Tasman Rise creates a sharper diffraction pattern, and
272 more back reflection. However, the REAL simulation has many of the same features as the RISE AND SHELF
273 simulation (figure 8c).

274 Slightly less incoming energy passes into the control volume (figure 11a) because the diffraction by the
275 real Tasman Rise is sharper than the cylindrical rise. As for the cylindrical rise case, there is some incoming
276 higher mode energy due to forward scattering, though again over 95% is mode-1. Reflection is concentrated
277 near $y = 125$ km and $y = 450$ km, associated with the diffraction nodes, with about 85% in mode 1
278 (figure 11b). Dissipation is less than 25% of the incoming energy (figure 11d).

279 **5. Discussion**

280 *a. Estimating reflection co-efficients*

281 A major goal of this effort is estimating the fraction of incoming tide that is reflected by the Tasman
282 continental slope to come up with a reflectivity co-efficient $R = F_{ref}/F_{in}$. Even here we need to be careful
283 to discriminate between the mode-1 reflection, $R_1 = F_{ref,1}/F_{in,1}$, and the total reflection into all the modes,
284 $R_T = F_{ref}/F_{in}$. Evaluating these co-efficients is less straightforward than it may sound because it is difficult

285 to separate the incoming from reflected signal in complicated geometry, even in a fully resolved numerical
286 model, let alone in observations. Above, we used an integrated measure, comparing the incoming flux from
287 a model with no continental slope to one with a continental slope and integrating the fluxes over a control
288 volume from $y = 0$ to 400 km. This was an arbitrary choice, but yielded reflectivities of mode -1 internal tide
289 $R_1 = 0.65$ and the total internal tide of $R_T = 0.76$ (figure 11).

290 Determining reflectivity from a mooring array is significantly complicated by three-dimensionality and
291 along slope variability. From the mooring array in figure 11, the reflectivity is $R_1 = 0.6/1.3 = 0.46$, a
292 significant under-estimate. The reason for this should be relatively clear from looking at figure 11a,b; the
293 mooring array nicely captures the northward diffracted ray, but catches some of the reflected pattern from
294 the main beam to the south. There are significant interferences in the reflected patterns (figure 11b) because
295 the reflected pattern is a complicated superposition of the cylindrically spreading reflections along the slope.

296 Determining the reflectivity as a function of along-slope direction y is difficult. Simply lining up the
297 onslope fluxes x -direction) does not yield useful results because the reflection from any given point on the
298 slope radiates cylindrically, and it is necessary to integrate over volumes. Here we take the same approach
299 as used in the previous section (i.e. figure 11), but integrate over smaller control volumes (80 km in y) to see
300 the reflectivity as a function of y (figure 12a,b). The incoming flux every 80 km shows the diffracted beam
301 pattern with a maximum net incoming flux at $y = 120\text{km}$ (figure 12a, red line) and a secondary peak to
302 the north at about 440 km. The net reflectivity from these boxes ranges from 0.8 to a low of almost zero at
303 $y = 280$ km (figure 12b, solid blue line). Note an uncertainty in the flux decomposition associated with the
304 flux in the cross terms (figure 12a, purple line). This term does not balance to zero, and forms a significant
305 part of the energy budget over such small control volumes. It cannot be uniquely decomposed into either
306 the incoming or reflected energy terms, so remains as an uncertainty.

307 The fraction of the tide reflected into mode 1 (and higher) can be predicted from linear theory using
308 the method described by Kelly et al. (2013b) of matching Laplacian tidal solutions at discrete steps on a
309 discretized topography. In two-dimensions an oblique incidence to the tide can make a substantial difference
310 in the modal distribution of the reflected tide (Kelly et al. 2013c). If we run these solutions for the Tasman
311 Slope with an incident angle of 30 degrees, the reflectivity into mode-1, R_1 is similar to the numerical

312 simulation (figure 12b, thick black line). The predicted reflectivity is greater for most of the ridge, but the
313 null at $y = 250$ km is captured.

314 The REAL simulation has a mode-1 reflectivity of $R_1 = 0.65$. A naive average of the reflectivity from the
315 linear model between $y = 0$ and 400 km yields $\langle R_1 \rangle = 0.71$. However, that does not take into account the
316 varying strength of the incoming diffracted beam, which is stronger where the reflectivity is higher. Weighting
317 by the incoming beam strength, then the reflectivity averages $\langle R_1 \rangle_{beam} = 0.8$, and is substantially larger
318 than in the numerical simulations.

319 An attempt has been made to estimate reflectivity from this site from autonomous gliders surveys at
320 this site(Johnston et al. 2015). First, the gliders saw a substantial concentration of energy shoreward of
321 the Tasman Rise. This is a feature of the model, and clearly explained by the diffraction of energy by the
322 Tasman Rise (figure 11).

323 For the region in the lee of the Tasman Rise, Johnston et al. (2015) estimate a reflectivity of the mode-1
324 internal tide of between 0.8 to 1.0 by fitting plane waves to the velocity and displacement amplitudes and
325 phases. If we confine our incoming versus outgoing energy budget to the region $80 \text{ km} < y < 200 \text{ km}$,
326 representative of their *Spray 56* deployment, we calculate a reflectivity of 0.7, which is lower than their
327 lowest estimate of 0.8, and much lower than their high estimate of 1.0. A second deployment, *Spray 55*,
328 covered more of the slope (up to $y = 300$ km). In this domain, they estimate a reflectivity of 0.6. This is in
329 agreement with the numerical simulation, which achieves the same result from $0 \text{ km} < y < 300 \text{ km}$.

330 The directions of wave propagation fit from the glider data is not in agreement with the model. The fits
331 to the *Spray 55* data show incoming energy at between 125 and 145 degrees, which is similar to the model.
332 However the reflection is slightly south of due east (0 to -30 degrees geographic), whereas the numerical
333 model is definitely to the north east far from shore. An explanation is evident from close inspection of
334 figure 11b between the Tasman Rise and the continental slope where the glider spent the most time. At this
335 location the off-shore energy flux is almost exactly in the x-direction, (-12 degrees geographic), in agreement
336 with the glider observations.

337 Finally, one of the gliders (*Spray 56*) picked out a northward propagating disturbance along the conti-
338 nental slope with wavelength of 100 km. This wavelength matches the wavelength of the slope wave seen in

339 the real simulations (figure 5a,b). Interestingly, they only pick this wavelength out in vertical displacement
340 data, not in velocity.

341 *b. Slope wave importance and dynamics*

342 The structure of the barotropic-to-baroclinic conversion on the slope is an intriguing feature of these
343 simulations, and appears in regional simulations (Simmons, in prep) and the glider data (Johnston et al.
344 2015). Here, it shows up most clearly in the SHELF simulations because of the simplified bathymetry.
345 However, it is also clear in the REAL simulation (figure 5a). This slope wave redistributes energy in the
346 reflected baroclinic response (figure 9), taking a relatively homogenous incoming energy source and focusing
347 the reflection every 200 km or so along shelf.

348 This wave is a slope mode that is strummed by the incident internal tide at the “corner” of the topography
349 ($x = 0$, $y = 0$); a long shelf without the corner does not excite this wave, nor does an internal tide
350 coming directly from the east and hitting the topography at a normal angle. The along-slope wavelength is
351 independent of the incident along-slope wavelength in the open water (tested by changing the angle of the
352 incident tide), and is a robust feature of the shelf shape. A sensitivity experiment that varied the continental
353 slope widths demonstrates that narrower slopes strum longer along-slope waves (figure 13).

354 These waves are super-inertial and are an example of partially trapped slope waves (Dale and Sherwin
355 1996; Dale et al. 2001). We compare the wavelength of the slope waves (figure 14, thick lines) to the empirical
356 modes predicted from linear theory (Dale et al. 2001). The procedure solves for the response of the flow in
357 the coastal cavity due to arbitrary forcing and find peaks in the response as the along-slope wavenumber is
358 changed (Appendix and figure 14, thin lines). The resonant modes agree quite well with the fully non-linear
359 solutions, and the spatial modes that correspond to the peaks are similar to deep-ocean mode-1 off the slope.

360 The shelf wave is an important term in the local energy budget when compared the incoming and
361 reflected energy fluxes (figure 15). The incoming energy peaks at 1.2 kW/m, and the reflected energy is
362 of a similar magnitude but with oscillations at twice the wavelength of the shelf wave. The integrated
363 barotropic-baroclinic conversion is as high as 0.4 kW/m, and leads to 0.4 kW/m peak-to-peak oscillation in
364 the reflected energy (its not 0.8 kW/m peak-to-peak because the reflected energy spreads spherically by 40

365 km, where the reflected flux is evaluated figure 9). This turns even a relatively straight shelf into a series of
366 internal tide absorbers and radiators, leading to 100-km scale inhomogeneity in the reflected internal tide.

367 6. Summary

368 A mode-1 internal tide was launched at a variety of topographies representing the Tasmanian continental
369 slope. The goal was to determine the “reflectivity” of this slope, in terms of the modal content of the
370 reflected energy and the local dissipation. The latter is somewhat suspect in this model because of crude
371 lateral resolution, but the REAL simulation indicated that 21% of the incoming energy was dissipated, and
372 65% was reflected as mode-1 energy. The incoming internal tide flux used here was weak compared to the
373 flux modeled and inferred from altimetry in the Tasman Sea, so we expect the dissipation in more strongly
374 forced models to increase.

375 Despite a relatively simple incoming internal tide which is linear, semi-diurnal, and mode-1, we have
376 found a rich and complex response of the topography when the remote wave impacts the topography east
377 of Tasmania. The response can be characterized as follows:

- 378 • Diffraction of the beam by the Tasman Rise,
- 379 • oblique reflection from the continental slope,
- 380 • and a leaky slope wave response that redistributes reflected internal energy along-slope.

381 Of these, perhaps only the second effect was expected before carrying out the simulations. However, as we
382 saw above, even the reflection problem is significantly complicated in the presence of three-dimensionality,
383 such that it is difficult to determine the appropriate slope for the incoming wave to impact the shelf.

384 Diffraction around underwater topography should have been expected, however, the relative depth of
385 the obstacle makes it surprising that the effect is so strong. The fact that the size of the Tasman Rise is
386 close to that of a wavelength of the incoming internal tide makes predicting the diffraction pattern difficult.
387 Baines (2007) considers generation of internal tides at seamounts, but does not deal with scattering and
388 diffraction. The problem is similar to electromagnetic waves passing through a wire, but a linear response

389 for that problem is not trivial to compute (i.e. Bonod et al. 2005), and still does not have a confined vertical
390 mode structure as we find in the internal wave problem.

391 The excitation of slope waves has been explored by Dale et al. (2001). It has an important effect on the
392 redistribution of energy along slope. The redistribution affects where high dissipation is found in the model
393 (figure 5), and adds more inhomogeneity to the reflected internal tide.

394 The complexity grows if other real-world influences are to be accounted for. The East Australian Current
395 flows along this slope, varying the stratification in the horizontal, provides lateral shears that can distort the
396 internal tide response, and carrying eddies that can add a strong time dependence to these effects. Even in
397 two dimensions, the strength of the internal tide reflection can be significantly impacted by the phase of the
398 incoming tide with other baroclinic modes Klymak et al. (2011) or the barotropic (Kelly and Nash 2010). The
399 simulations here exclude the local barotropic tide, so this would certainly complicate the reflected response.
400 Finally, the internal tide used here was monotonic, whereas the real tide will have other frequencies, most
401 notably subinertial diurnal frequencies that will have trapped wave responses (personal communication, R.
402 Musgrave).

403 Regardless, it is useful to have separated the “simplest” response we could in this system to tease apart the
404 dominant physics. This response is complex enough as it is that it should be clear that solely observational
405 efforts to balance a reflection budget are going to be a challenge. Merging simulations and observations is a
406 likely way forward in understanding the wave field in this complex slope region.

407 With respect to the reflection problem, the modeled slope has a relatively high reflection back into the
408 open ocean, with as much as 65% of the incoming energy being reflected as mode-1. Its possible that higher
409 resolution runs will be more dissipative, and that stronger forcing will lead to a higher fraction of dissipation.
410 However, these simulations, and the results from the rest of the experiment to date (i.e. Johnston et al. 2015)
411 indicate that bulk of the energy from the Macquarie Ridge must dissipate elsewhere.

412 *Acknowledgments.*

413 Start acknowledgments here.

APPENDIX

416 Appendix Slope-wave calculation

417 The slope wave calculation follows the calculation made by Dale et al. (2001), where there are more details.

418 The linear equation for the pressure perturbations are assumed to have form $P = p(x, z) \exp^{i(k_y y - \omega t)}$, where

419 k_y is the along-slope wavenumber.

$$(f^2 - \omega^2) \frac{\partial}{\partial z} \left(\frac{\partial p / \partial z}{N^2 - \omega^2} \right) + \frac{\partial^2 p}{\partial x^2} - k_y^2 p = 0 \quad (\text{A1})$$

420 Subject to boundary conditions at the surface of $\partial p / \partial z = 0$ and at the sea floor of

$$\left(\frac{\omega^2 - f^2}{N^2 - \omega^2} \right) \frac{\partial p}{\partial z} = \frac{\partial h}{\partial x} \left(\frac{\partial p}{\partial x} - \frac{f k_y}{\omega} p \right) \quad (\text{A2})$$

421 The coast is assumed to be a wall, and the open ocean to consist of waves radiating away from the slope, or

422 if k_x , the cross-slope wavenumber, is imaginary, disturbances that decay away from the slope.

423 The above are discretized on a domain that is 260 km wide into 261 grid cells in x , and onto a sigma-

424 co-ordinate with 192 vertical levels. The hyperbolic method of solution due to Lindzen and Kuo (1969) was

425 used to solve on this domain for p for $\omega = 1.4f$, $f = 10^{-4}\text{s}^{-1}$, and for a sweep of k_y . Under an arbitrary

426 forcing certain values of k_y resonate and lead to stronger amplitude responses in p corresponding to spatial

427 modes of the system. The numerical method is sensitive to the stratification, so we used a fit exponential of

428 $N^2(z) = 2 \times 10^{-5}\text{s}^{-2} e^{z/(1000 \text{ m})}$ (where z is negative downwards). The scan was taken over 300 wavelengths

429 equally spaced between 30 and 180 km.

430 The resulting spatial modes are similar to those in Dale et al. (2001) (figure 16). There is a peak of

431 amplitude on the shelf, and then a second peak on the slope. As the slope gets more narrow, the peak on

432 the slope becomes broader. These shapes are the lowest modes.

433 The general code to solve this is at <https://github.com/jklymak/LindzenKuo>. The exact code used

434 for this paper is with the rest of the supplemental material.

REFERENCES

- 437 Baines, P. G., 2007: Internal tide generation by seamounts. *Deep Sea Res. I*, **54** (9), 1486 – 1508, doi:
 438 <http://dx.doi.org/10.1016/j.dsr.2007.05.009>, URL <http://www.sciencedirect.com/science/article/pii/S0967063707001306>.
- 440 Bonod, N., E. Popov, and M. Nevière, 2005: Differential theory of diffraction by finite cylindrical objects.
 441 *JOSA A*, **22** (3), 481–490.
- 442 Boyer, T., et al., 2013: *World Ocean Database 2013*. NOAA Atlas NESDIS 72, doi:10.7289/V5NZ85MT.
- 443 Buijsman, M. C., et al., 2014: Three-dimensional double-ridge internal tide resonance in Luzon Strait. *J.
 444 Phys. Oceanogr.*, **44** (3), 850–869.
- 445 Carter, G., et al., 2008: Energetics of M 2 Barotropic-to-Baroclinic Tidal Conversion at the Hawaiian Islands.
 446 *Journal of Physical Oceanography*, **38** (10), 2205–2223.
- 447 Dale, A. C., J. M. Huthnance, and T. J. Sherwin, 2001: Coastal-trapped waves and tides at near-inertial
 448 frequencies. *J. Phys. Oceanogr.*, **31** (10), 2958–2970.
- 449 Dale, A. C. and T. J. Sherwin, 1996: The extension of baroclinic coastal-trapped wave theory to superinertial
 450 frequencies. *J. Phys. Oceanogr.*, **26** (11), 2305–2315.
- 451 Hall, R. A., J. M. Huthnance, and R. G. Williams, 2013: Internal wave reflection on shelf slopes with
 452 depth-varying stratification. *J. Phys. Oceanogr.*, **43** (2), 248–258.
- 453 Johnston, T. M. S., D. L. Rudnick, and S. M. Kelly, 2015: Standing internal tides in the Tasman Sea
 454 observed by gliders, doi:<http://www-pord.ucsd.edu/~shaunj/files/standing20150528.pdf>, in press *J. Phys.
 455 Oceanogr.*
- 456 Johnston, T. S. and M. A. Merrifield, 2003: Internal tide scattering at seamounts, ridges, and islands. *J.
 457 Geophys. Res.*, **108** (C6), 3180, doi:10.1029/2002JC01528.

- 458 Kang, D., 2011: Barotropic and baroclinic tidal energy. Ph.D. thesis, Stanford University.
- 459 Kang, D. and O. Fringer, 2012: Energetics of barotropic and baroclinic tides in the monterey bay area. *J.
460 Phys. Oceanogr.*, **42** (2), 272–290.
- 461 Kelly, S. and J. Nash, 2010: Internal-tide generation and destruction by shoaling internal tides. *Geophysical
462 Research Letters*, **37**, L23 611.
- 463 Kelly, S. M., N. L. Jones, and J. D. Nash, 2013a: A coupled model for laplace's tidal equations in a fluid
464 with one horizontal dimension and variable depth. *Journal of Physical Oceanography*, **(2013)**.
- 465 Kelly, S. M., N. L. Jones, and J. D. Nash, 2013b: A coupled model for laplace's tidal equations in a
466 fluid with one horizontal dimension and variable depth. *Journal of Physical Oceanography*, **(2013)**, doi:
467 10.1175/JPO-D-12-0147.1.
- 468 Kelly, S. M., N. L. Jones, J. D. Nash, and A. F. Waterhouse, 2013c: The geography of semidiurnal mode-1
469 internal-tide energy loss. *Geophys. Res. Lett.*, doi:10.1002/grl.50872, URL <http://dx.doi.org/10.1002/grl.50872>.
- 470
- 471 Klymak, J., M. Alford, R. Pinkel, R. Lien, Y. Yang, and T. Tang, 2011: The breaking and scattering of the
472 internal tide on a continental slope. *J. Phys. Oceanogr.*, **41**, 926–945, doi:10.1175/2010JPO4500.1.
- 473 Klymak, J. M. and S. M. Legg, 2010: A simple mixing scheme for models that resolve breaking internal
474 waves. *Ocean Modell.*, **33** (3-4), 224 – 234, doi:10.1016/j.ocemod.2010.02.005.
- 475 Klymak, J. M., et al., 2006: An estimate of tidal energy lost to turbulence at the Hawaiian Ridge. *J. Phys.
476 Oceanogr.*, **36**, 1148–1164.
- 477 Legg, S. and J. M. Klymak, 2008: Internal hydraulic jumps and overturning generated by tidal flow over a
478 tall steep ridge. *J. Phys. Oceanogr.*, **38** (9), 1949–1964.
- 479 Lindzen, R. and H.-L. Kuo, 1969: A reliable method for the numerical integration of a large class of ordinary
480 and partial differential equations. *Mon. Wea. Rev.*

- 481 Marshall, J., E. Shuckburgh, H. Jones, and C. Hill, 2006: Estimates and implications of surface eddy
482 diffusivity in the Southern Ocean derived from tracer transport. *J. Phys. Oceanogr.*, **36** (9), 1806–1821.
- 483 Martini, K., M. Alford, J. Nash, E. Kunze, and M. Merrifield, 2007: Diagnosing a partly standing internal
484 wave in Mamala Bay, Oahu. *Geophys. Res. Lett.*, **34** (17), L17604.
- 485 Martini, K. I., M. H. Alford, E. Kunze, S. M. Kelly, and J. D. Nash, 2013: Internal bores and breaking
486 internal tides on the oregon continental slope. *J. Phys. Oceanogr.*, **43**, 120–139.
- 487 Melet, A., R. Hallberg, S. Legg, and K. Polzin, 2013: Sensitivity of the ocean state to the vertical distribution
488 of internal-tide-driven mixing. *J. Phys. Oceanogr.*, **43** (3), 602–615.
- 489 Mercier, M. J., N. B. Garnier, and T. Dauxois, 2008: Reflection and diffraction of internal waves analyzed
490 with the Hilbert transform. *Phys. Fluids*, **20** (8), 086601.
- 491 Nash, J., M. Alford, E. Kunze, K. Martini, and S. Kelley, 2007: Hotspots of deep ocean mixing on the
492 Oregon continental slope. *Geophys. Res. Lett.*, **34**, L01605, doi:10.1029/2006GL028170.
- 493 Nash, J. D., E. Kunze, J. M. Toole, and R. W. Schmitt, 2004: Internal tide reflection and turbulent mixing
494 on the Continental Slope. *J. Phys. Oceanogr.*, 1117–1134.
- 495 Polzin, K. L., 2009: An abyssal recipe. *Ocean Modelling*, **30** (4), 298–309, doi:doi:10.1016/j.ocemod.2009.
496 07.007.
- 497 Rainville, L., T. Johnston, G. S. Carter, M. A. Merrifield, R. Pinkel, P. F. Worcester, and B. D. Dushaw,
498 2010: Interference pattern and propagation of the m2 internal tide south of the hawaiian ridge. *J. Phys.*
499 *Oceanogr.*, **40** (2).
- 500 Smith, W. and D. Sandwell, 1997: Global sea floor topography from satellite altimetry and ship depth
501 soundings. *Science*, **277** (5334), 1956.
- 502 St. Laurent, L. and C. Garrett, 2002: The role of internal tides in mixing the deep ocean. *J. Phys. Oceanogr.*,
503 **32**, 2882–2899.

- 504 Whiteway, T., 2009: Australian bathymetry and topography grid, june 2009. scale 1:5000000. Tech. rep.,
505 Geoscience Australia, Canberra. doi:10.4225/25/53D99B6581B9A.
- 506 Zhao, Z. and M. H. Alford, 2009: New altimetric estimates of mode-1 M2 internal tides in the central North
507 Pacific Ocean. *J. Phys. Oceanogr.*, **39** (7), 1669–1684.

508 **List of Figures**

- 509 1 Schematic of the difficulty of quantifying reflecting fluxes in an inhomogeneous environment.
510 Plane waves are trivial. Inhomogeneous incoming waves or reflections are significantly more
511 difficult. 26
- 512 2 Location of TTide experiment: a) Energy flux in a regional numerical simulation. Color is
513 the absolute value of the flux, arrows its direction. The magenta box indicates the numerical
514 modeling domain used in this paper. b) Detail of the bathymetry on the Tasman slope. The
515 magenta lines indicate 100 km in the x-direction, and 300 km in the y direction in the modeling
516 domain used in this paper. 27
- 517 3 a) Forcing used to drive the models used in this paper. Two mode-1 internal wave sources
518 are located to the south east (blue lines). The model domain is rotated 12 degrees from
519 geographic so the shelf break approximately lies along $x = 0$. Typical model domain and
520 sponge region is indicated as green rectangles. The 250, and 3000-m isobaths are contoured.
521 Arrows show the direction of the energy flux, and are scaled by its strength. b) Energy flux
522 of analytical response of energy reflecting from a wall at $x = 0$, north of $y = 0$. c) Phase of
523 reflected response. 28
- 524 4 a)-d) Surface x-direction velocity for four snapshots. a) is the initial conditions (slightly
525 modified after a tidal cycle) and d) is the steady state. Grey contours are depths at 3000,
526 2000, 1000, and 250-m. e)-h) is depth-integrated baroclinic energy flux at the same time
527 periods, with arrows indicating direction. 29
- 528 5 Energy budget over the 19th tidal cycle of a) Barotropic to baroclinic conversion; b) Baro-
529 clinic energy flux convergence ($-\nabla F_{bc}$); c) rate of change of baroclinic energy; d) residual
530 representing the dissipation in the model $D = -\nabla \mathbf{F}_{bc} + \text{Conv.} - dE/dt$. The green box is the
531 region for the energy time series (figure 6b). 30

532 6 a) Integral in x to 80 km offshore of the energy terms in figure 5 for the REAL case. Note
533 that the barotropic-baroclinic term (red) is of the same order as the baroclinic convergence
534 (cyan) and the residual dissipation (gray) for most of the shelf. b) Energy budget time series
535 for the “Real” case, tidally averaged, where time is normalized by $T = 12.4h$, between $y = 0$
536 to $y = 400$ km. There is still a small residual increase in the energy with time (purple),
537 representing the accumulation of high-mode energy in the region. Net barotropic-baroclinic
538 conversion (red) is small and negative, indicating a small net loss to the barotropic tide in
539 this region. The bulk of the budget is the balance between baroclinic flux convergence (blue)
540 and the residual “dissipation” (gray). c) Net flux in the box defined by $0 < x < 80$ km, and
541 $0 < y < 400$ km. Green is the value for the net flux (no modal decomposition). Blue bars are
542 the modal decomposition. There is a net incoming flux in mode 1 and net reflecting fluxes in
543 higher modes (primarily modes 2-4).

31

544 7 Cross sections of topographies from $y = 50$ km.

32

545 8 Energy flux for six geometries at tidal cycle 20. Grey depth contours are -3000, -2000, -1000
546 and -250 m. Arrows indicate the direction of energy flux. See figure 7 for bathymetry cross
547 sections at $y = 50$ km.

33

548 9 Mode-1 decomposition of energy fluxes for the SHELF experiment. a) Incoming energy flux
549 calculated from the No TOPO simulation (figure 8a). Note that the shelf bathymetry is
550 contoured on this plot (grey lines, and green “land”), but this bathymetry was not part
551 of this simulation. The green line demarks the region the energy budget in the inset was
552 integrated over. The green diamonds are the location of a synthetic mooring, and the arrow
553 indicates the estimated incoming flux from a plane wave fit over the three moorings of the
554 “Total” simulation (see text). b) Reflected energy flux calculated from the difference between
555 the velocities and displacements of the Total simulation (panel d) and the “Incoming” (panel
556 a). Blue arrow is the outgoing flux from a plane wave fit over the mooring array from the
557 “Total” simulation. c) Energy flux cross terms between the incoming and outgoing waves. d)
558 Total simulation from the SHELF case (figure 8d)

34

559 10 Mode-1 decomposition of energy fluxes for the RISE-SHELF experiment. 35

560 11 Energy decomposition based on taking the NO TOPO case as the incoming wave, and RISE
561 as the total wavefield and looking at the energy flux of the difference between their waves
562 (reflected wave field) and the energy flux associated with the cross terms between. 36

563 12 a) Energy budget from 80 km by 80 km control volumes along the continental slope from the
564 REAL simulations. The incoming flux (red) is compared to the reflected (blue) and the cross
565 terms (purple). b) The reflection co-efficients. The blue line is R_1 , the mode-1 reflectivity in
566 the 80-km control volumes along slope from the non-linear simulation. The black line is the
567 mode-1 reflectivity from a linear model (Kelly et al. 2013b), and the grey lines behind are the
568 cumulative sum of modes 2, to 5 and then all the modes. These do not sum up to one because
569 the linear model has some “viscosity” that removes some high-mode energy. The dashed lines
570 are the mean of R_1 from the linear model if a constant average is taken (light blue, dashed),
571 and if weighted by the diffracted beam strength (purple, dashed). 37

572 13 Barotropic to baroclinic conversion for different shelf widths from widest (a) to narrowest (d).
573 Arrows are barotropic flux vectors. Note how the along-slope barotropic flux is almost entirely
574 confined to conversion dipoles along slope. 38

575 14 Along-slope spectra of across slope velocity (thick lines) for the three narrowest slopes in
576 figure 13, from velocities on the shallow shelf in these simulations. The thin lines are resonance
577 curves, formed from the cross-slope equations of motion assuming harmonic motion in time and
578 along-slope. As along-slope wavenumber is varied resonant modes have a stronger response.
579 What is plotted is arbitrary units for the three shelf geometries. 39

580 15 Terms from the energy budget for 40-km wide shelf along slope. The incoming and reflected
581 energy fluxes are computed at $x = 40$ km, and the conversion term integrated from the shelf
582 to $x = 40$ km. 40

583 16 Spatial shape of modes picked out from the resonant searching technique (as shown in fig-
584 ure 14) for the 70, 40 and 20-km wide slopes. 41

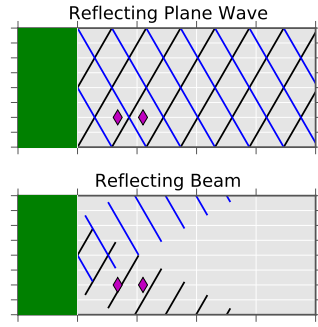


FIG. 1. Schematic of the difficulty of quantifying reflecting fluxes in an inhomogeneous environment. Plane waves are trivial. Inhomogeneous incoming waves or reflections are significantly more difficult.

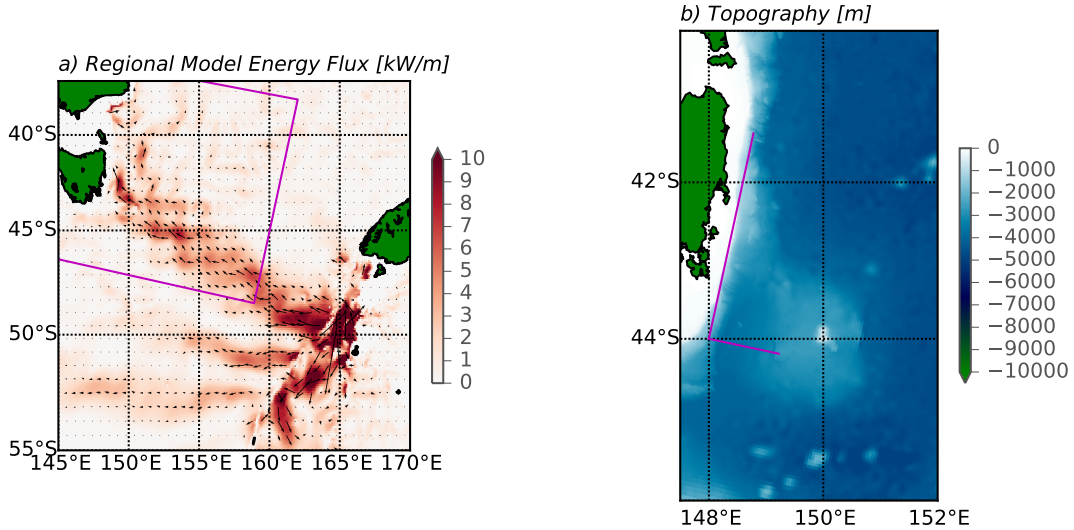


FIG. 2. Location of TTide experiment: a) Energy flux in a regional numerical simulation. Color is the absolute value of the flux, arrows its direction. The magenta box indicates the numerical modeling domain used in this paper. b) Detail of the bathymetry on the Tasman slope. The magenta lines indicate 100 km in the x-direction, and 300 km in the y direction in the modeling domain used in this paper.

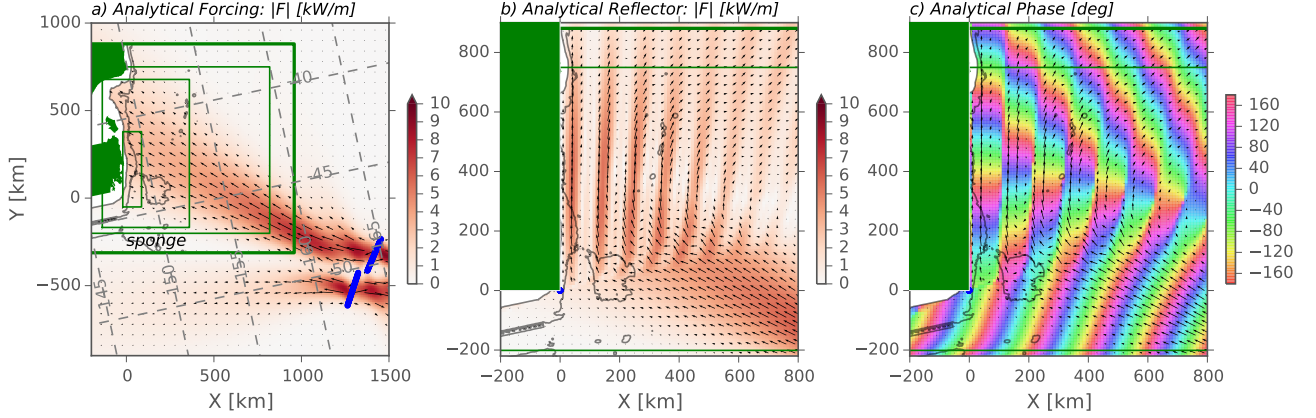


FIG. 3. a) Forcing used to drive the models used in this paper. Two mode-1 internal wave sources are located to the south east (blue lines). The model domain is rotated 12 degrees from geographic so the shelf break approximately lies along $x = 0$. Typical model domain and sponge region is indicated as green rectangles. The 250, and 3000-m isobaths are contoured. Arrows show the direction of the energy flux, and are scaled by its strength. b) Energy flux of analytical response of energy reflecting from a wall at $x = 0$, north of $y = 0$. c) Phase of reflected response.

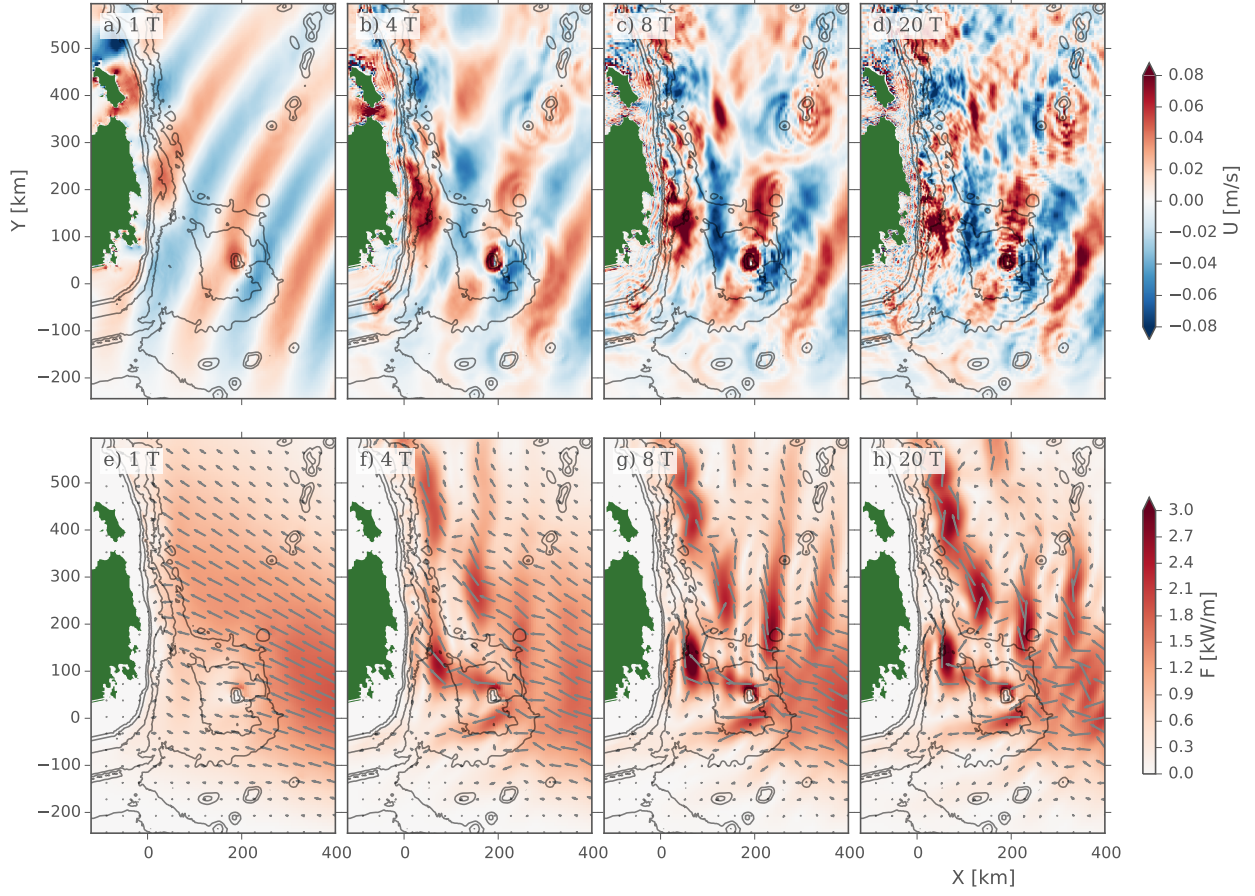


FIG. 4. a)-d) Surface x-direction velocity for four snapshots. a) is the initial conditions (slightly modified after a tidal cycle) and d) is the steady state. Grey contours are depths at 3000, 2000, 1000, and 250-m. e)-h) is depth-integrated baroclinic energy flux at the same time periods, with arrows indicating direction.

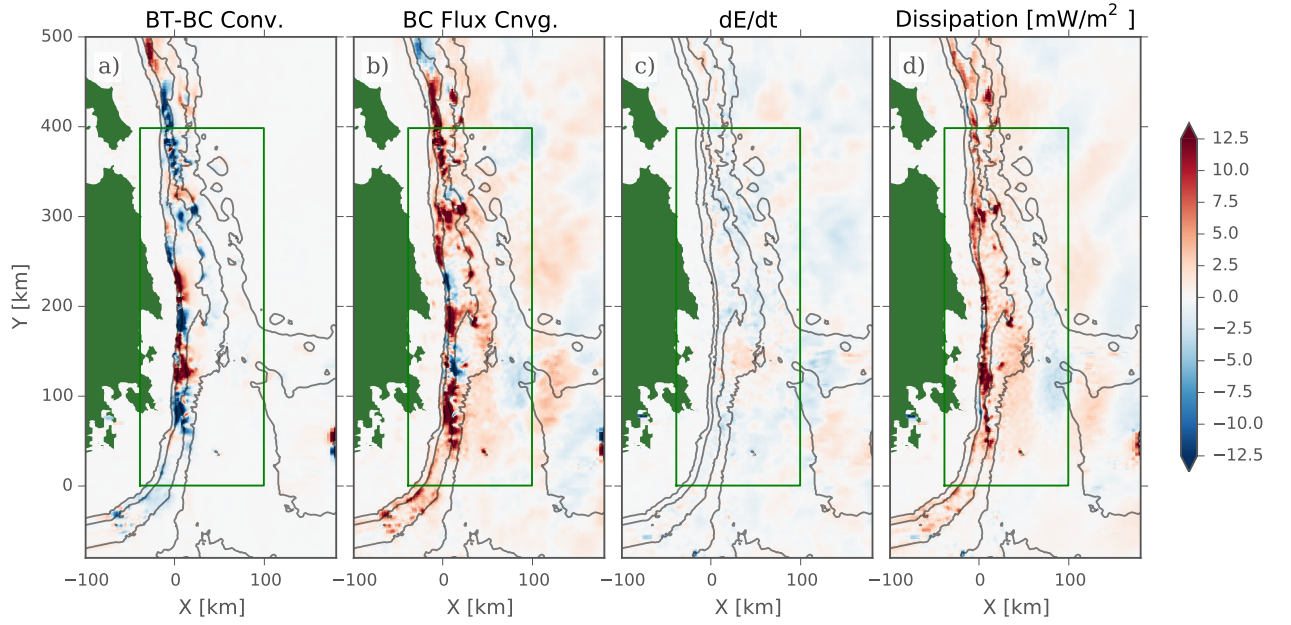


FIG. 5. Energy budget over the 19th tidal cycle of a) Barotropic to baroclinic conversion; b) Baroclinic energy flux convergence ($-\nabla F_{bc}$); c) rate of change of baroclinic energy; d) residual representing the dissipation in the model $D = -\nabla F_{bc} + \text{Conv.} - dE/dt$. The green box is the region for the energy time series (FIG. 6b).

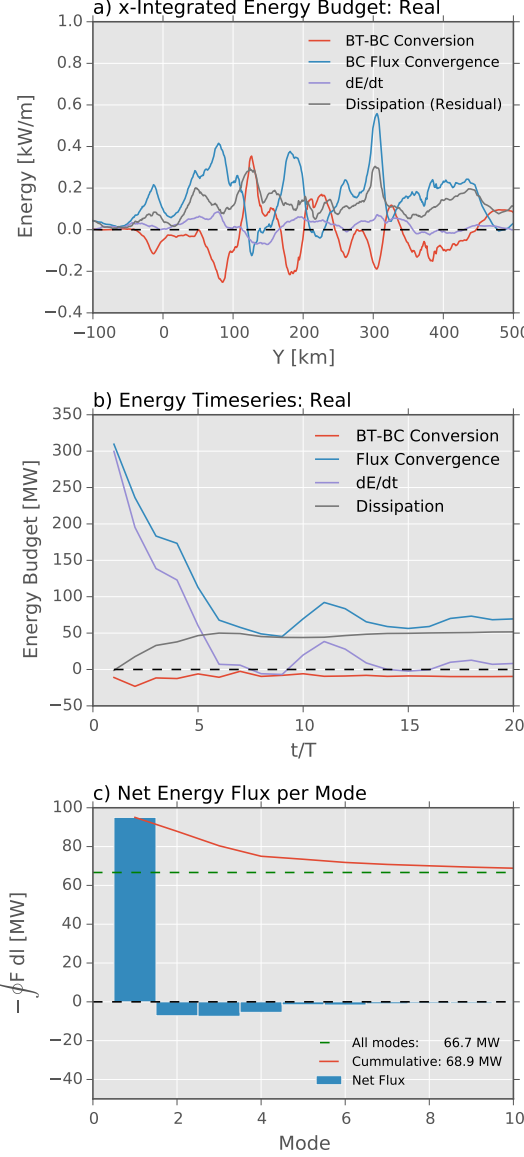


FIG. 6. a) Integral in x to 80 km offshore of the energy terms in FIG. 5 for the REAL case. Note that the barotropic-baroclinic term (red) is of the same order as the baroclinic convergence (cyan) and the residual dissipation (gray) for most of the shelf. b) Energy budget time series for the “Real” case, tidally averaged, where time is normalized by $T = 12.4h$, between $y = 0$ to $y = 400$ km. There is still a small residual increase in the energy with time (purple), representing the accumulation of high-mode energy in the region. Net barotropic-baroclinic conversion (red) is small and negative, indicating a small net loss to the barotropic tide in this region. The bulk of the budget is the balance between baroclinic flux convergence (blue) and the residual “dissipation” (gray). c) Net flux in the box defined by $0 < x < 80$ km, and $0 < y < 400$ km. Green is the value for the net flux (no modal decomposition). Blue bars are the modal decomposition. There is a net incoming flux in mode 1 and net reflecting fluxes in higher modes (primarily modes 2-4).

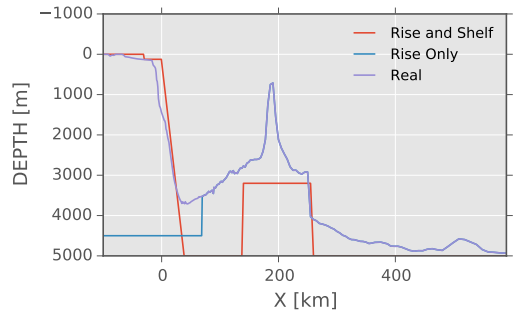


FIG. 7. Cross sections of topographies from $y = 50$ km.

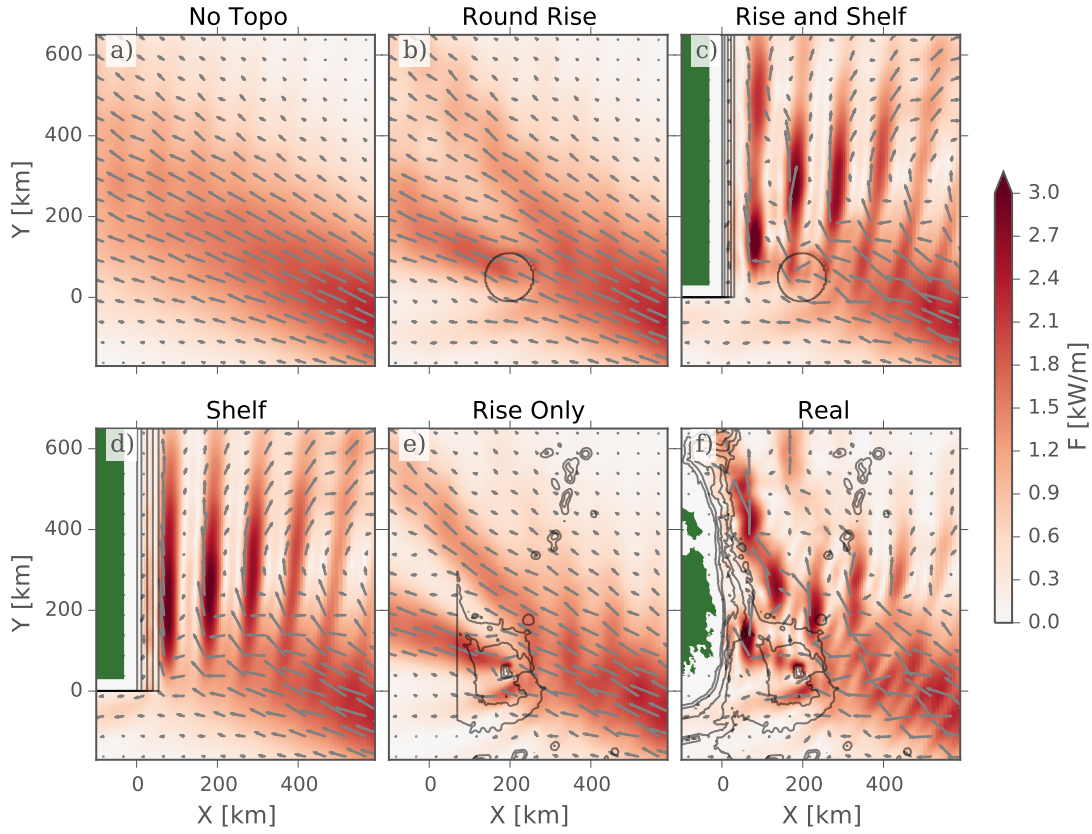


FIG. 8. Energy flux for six geometries at tidal cycle 20. Grey depth contours are -3000, -2000, -1000 and -250 m. Arrows indicate the direction of energy flux. See FIG. 7 for bathymetry cross sections at $y = 50$ km.

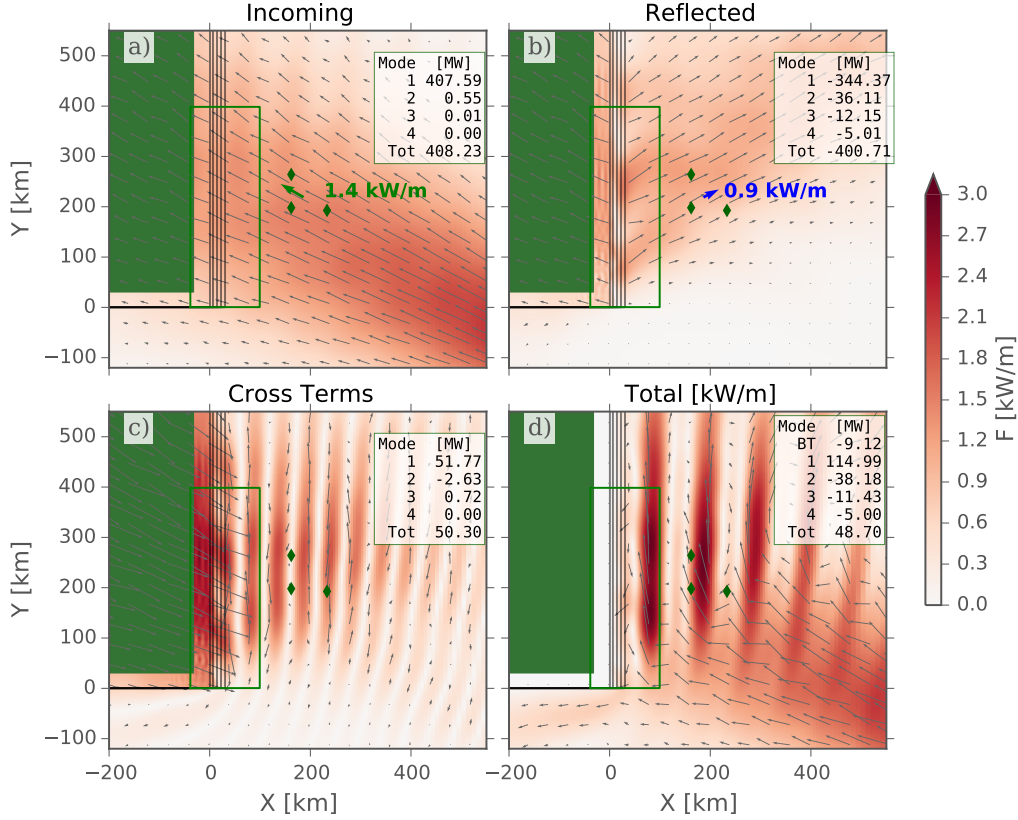


FIG. 9. Mode-1 decomposition of energy fluxes for the SHELF experiment. a) Incoming energy flux calculated from the NO TOPO simulation (FIG. 8a). Note that the shelf bathymetry is contoured on this plot (grey lines, and green “land”), but this bathymetry was not part of this simulation. The green line marks the region the energy budget in the inset was integrated over. The green diamonds are the location of a synthetic mooring, and the arrow indicates the estimated incoming flux from a plane wave fit over the three moorings of the “Total” simulation (see text). b) Reflected energy flux calculated from the difference between the velocities and displacements of the Total simulation (panel d) and the “Incoming” (panel a). Blue arrow is the outgoing flux from a plane wave fit over the mooring array from the “Total” simulation. c) Energy flux cross terms between the incoming and outgoing waves. d) Total simulation from the SHELF case (FIG. 8d)

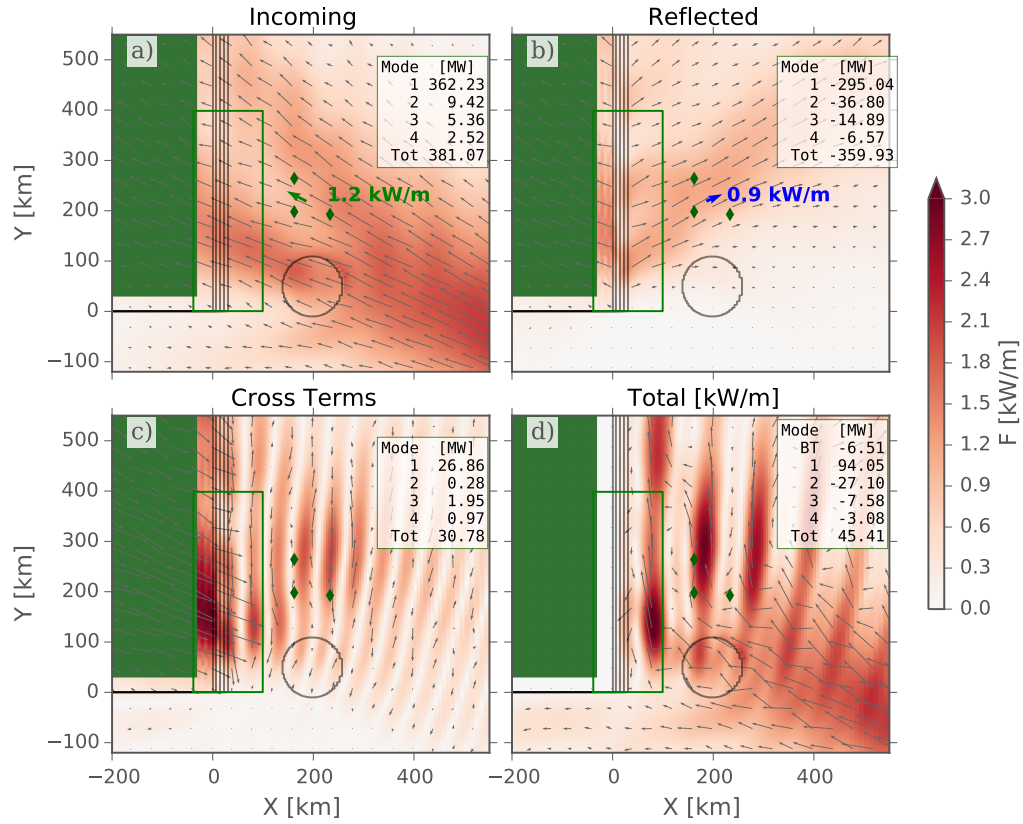


FIG. 10. Mode-1 decomposition of energy fluxes for the RISE-SHELF experiment.

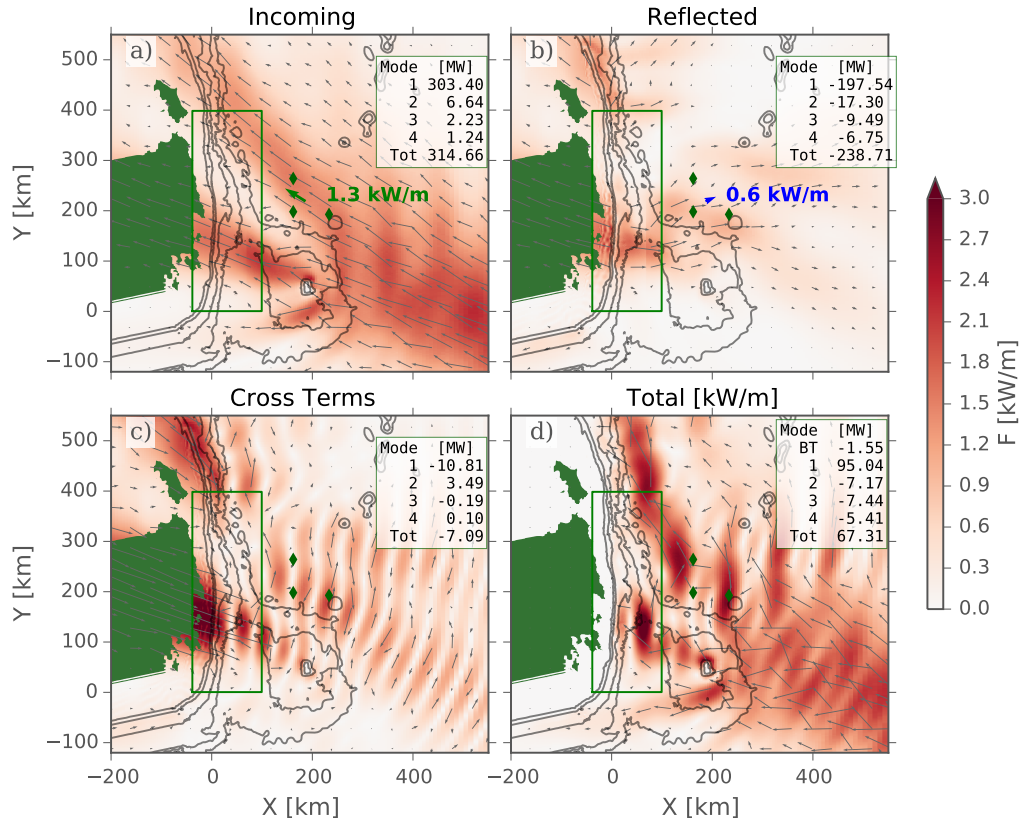


FIG. 11. Energy decomposition based on taking the No TOPO case as the incoming wave, and RISE as the total wavefield and looking at the energy flux of the difference between their waves (reflected wave field) and the energy flux associated with the cross terms between.

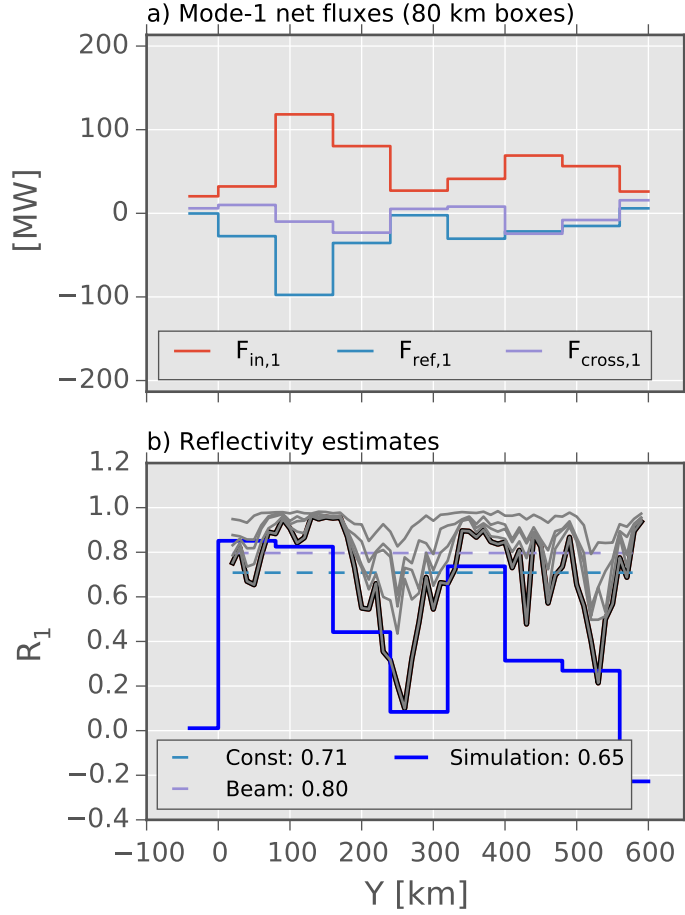


FIG. 12. a) Energy budget from 80 km by 80 km control volumes along the continental slope from the REAL simulations. The incoming flux (red) is compared to the reflected (blue) and the cross terms (purple). b) The reflection co-efficients. The blue line is R_1 , the mode-1 reflectivity in the 80-km control volumes along slope from the non-linear simulation. The black line is the mode-1 reflectivity from a linear model (Kelly et al. 2013b), and the grey lines behind are the cumulative sum of modes 2, to 5 and then all the modes. These do not sum up to one because the linear model has some “viscosity” that removes some high-mode energy. The dashed lines are the mean of R_1 from the linear model if a constant average is taken (light blue, dashed), and if weighted by the diffracted beam strength (purple, dashed).

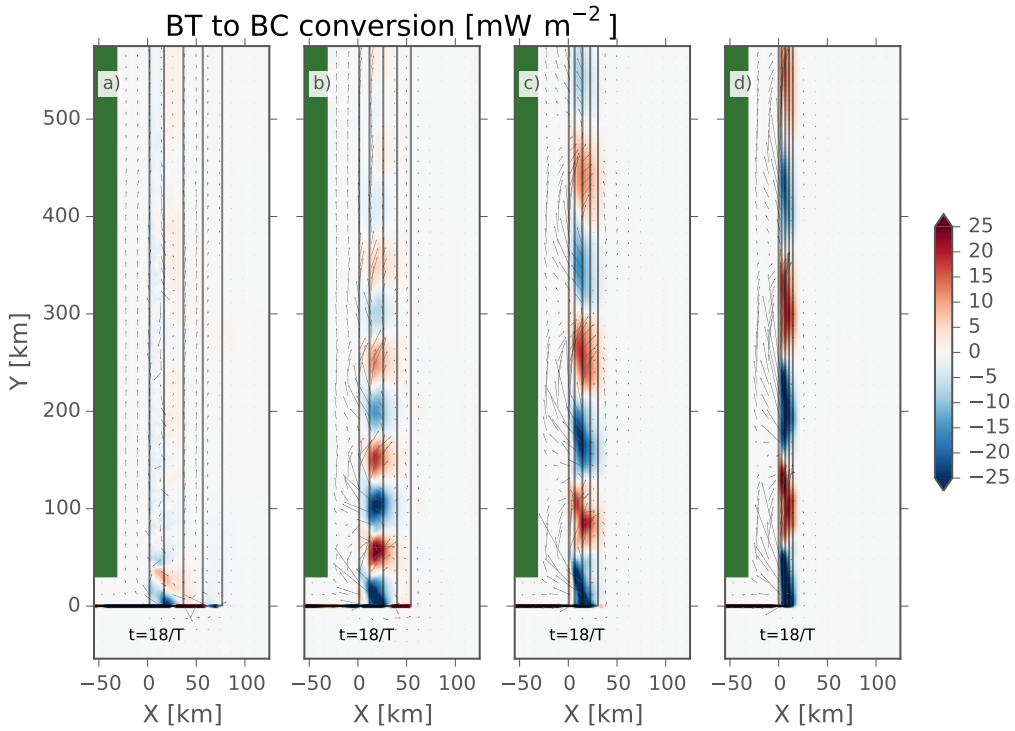


FIG. 13. Barotropic to baroclinic conversion for different shelf widths from widest (a) to narrowest (d). Arrows are barotropic flux vectors. Note how the along-slope barotropic flux is almost entirely confined to conversion dipoles along slope.

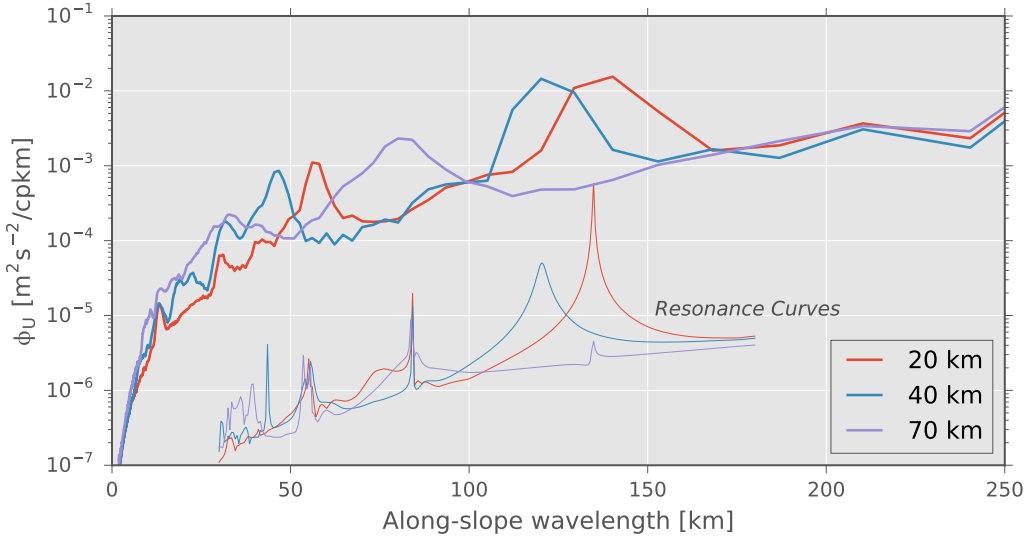


FIG. 14. Along-slope spectra of across slope velocity (thick lines) for the three narrowest slopes in FIG. 13, from velocities on the shallow shelf in these simulations. The thin lines are resonance curves, formed from the cross-slope equations of motion assuming harmonic motion in time and along-slope. As along-slope wavenumber is varied resonant modes have a stronger response. What is plotted is arbitrary units for the three shelf geometries.

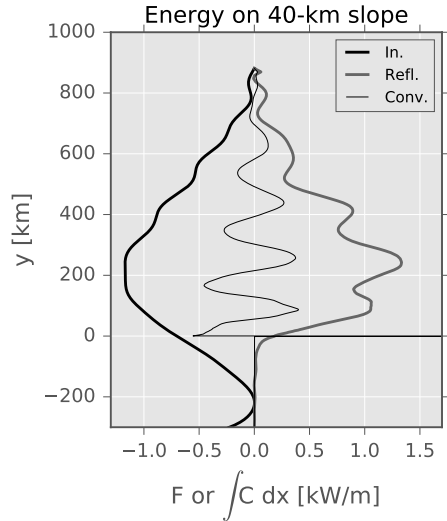


FIG. 15. Terms from the energy budget for 40-km wide shelf along slope. The incoming and reflected energy fluxes are computed at $x = 40$ km, and the conversion term integrated from the shelf to $x = 40$ km.

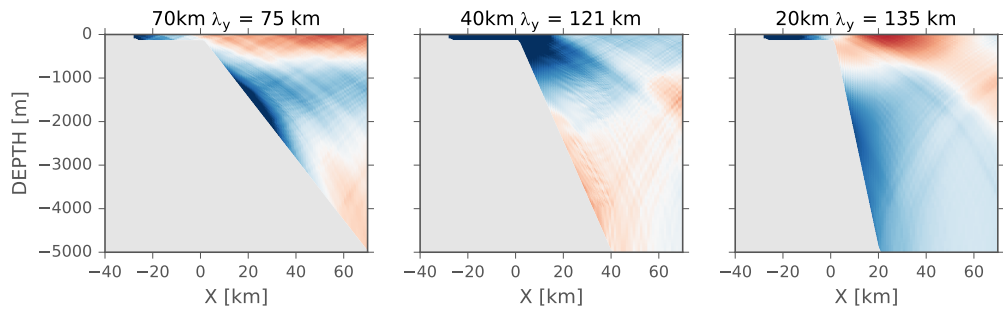


FIG. 16. Spatial shape of modes picked out from the resonant searching technique (as shown in FIG. 14) for the 70, 40 and 20-km wide slopes.